Available online at www.sciencedirect.com

ScienceDirect

Proceedings of the Combustion Institute 38 (2021) 6403–6411

Proceedings of the Combustion Institute

www.elsevier.com/locate/proci

Investigation of CO recombination in the boundary layer of CH_4/O_2 rocket engines

Nikolaos Perakis [a,b,*], Oskar J. Haidn [b], Matthias Ihme [a]

[a] *Department of Mechanical Engineering, Stanford University, Stanford, CA 94305, USA*
[b] *Chair of Space Propulsion, Technical University of Munich, Garching 85748, Germany*

Received 7 November 2019; accepted 19 July 2020
Available online 2 October 2020

Abstract

In this work, the combustion and thermal recombination in the boundary layer of a single-element methane/oxygen rocket combustor is investigated using large-eddy simulations. The experimental configuration consists of a coaxial injector and an operating point with a nominal pressure of 20 bar and gaseous injection of both propellants are considered. A non-adiabatic flamelet model is utilized with the purpose of examining its capability to predict the wall heat transfer. Good agreement of the simulation results with measurements of heat flux and pressure profiles is obtained using the non-adiabatic model. By comparing results with a frozen flamelet model, the importance of the recombination reactions in the cold boundary layer is investigated. The species profiles of CO and CO_2 are examined and the reaction pathways leading to the recombination reactions at the wall were analyzed. Results from this analysis show that the reaction of OH with CO forming CO_2 is the main contributor to the additional heat release in the boundary layer.

Keywords: Reacting boundary layer; Recombination reactions; Methane combustion; Heat transfer; Rocket engines

1. Introduction

In an effort to decrease launch costs and to design reliable and efficient propulsion systems for space applications, significant research efforts have been dedicated towards advancing the maturity level of the propellant combination methane/oxygen [1–3]. This interest in methane/oxygen is attributed to the fact that it offers improved performance with reusability, sustainability and a potential cost reduction compared to conventional propellants such as H_2 and RP-1 [4,5].

Over recent years, efforts have been dedicated towards developing improved modeling techniques for a reliable prediction of combustion performance in rocket motors. However, these investigations have mainly focused on the H_2/O_2 propellant combination [6,7], while investigations of methane remain limited.

Apart from typical performance metrics such as specific impulse, thrust and characteristic velocity, combustion models have to accurately predict the

* Corresponding author at: Department of Mechanical Engineering, Stanford University, Stanford, CA 94305, USA.
E-mail address: nikolaos.perakis@tum.de (N. Perakis).

https://doi.org/10.1016/j.proci.2020.07.080
1540-7489

wall heat loads, which is of major interest in the design of rocket engines. Given the extreme heat flux values occurring at the walls of rocket thrust chambers, reaching up to 150 MW/m^2 [8], understanding the flame-wall interaction is crucial. To avoid mechanical failure of the chamber and to reduce uncertainties of the operational lifetime of the engine, a precise knowledge of the spatial distribution of the thermal load is necessary [9,10].

Compared to hydrogen, the combustion of methane evolves on slower chemical time scales, resulting in the formation of a non-equilibrium chemical state in the boundary layer at the cooled chamber wall, which requires additional modeling. Due to the wall heat loss, the hot combustion products inside the thrust chamber are abruptly cooled within the thermal boundary layer. This enthalpy reduction induces chemical reactions that enhance the wall heat flux and therefore influence the design of the cooling system and the overall cycle performance [11]. Several studies were conducted to examine the aforementioned reactions and to extend existing combustion models. Cabrit et al. [12] performed direct numerical simulations and wall-resolved large-eddy simulation (LES) of a turbulent reacting channel flow, but the operating point was not directly relevant for rocket conditions. More recently, Betti et al. [13] investigated effects of recombination reactions on the wall heat loads of methane/oxygen engines with relevance to rocket combustion. Efforts to incorporate effects of wall heat transfer in flamelet-models have been conducted. These developments include work by Ma et al. [14] in which heat loss is modeled via a permeable wall in the counterflow diffusion problem and applying the model to predict the heat loads of an H_2/O_2 rocket engine. Breda et al. [15] applied the same model in simulations of a sub-scale CH_4/O_2 rocket engine, whereas Perakis et al. [16] developed an enthalpy-constrained extension of the flamelet model to account for the recombination reactions. Furthermore, Zips et al. [17] and Maestro et al. [18] predicted the wall heat flux distribution in sub-scale methane/oxygen rocket engines using LES.

Previous studies have identified the recombination of CO and CO_2 as a main mechanism leading to an increase in the wall heat flux of hydrocarbon engines [13,16]. However their is a lack of fundamental understanding and predictive modeling of this effect.

The objective of the present investigation is to evaluate the ability of a non-adiabatic flamelet model to capture the recombination reactions at the wall and to predict the wall-heat transfer. By addressing this need, a validation of the model is carried out and the LES results are examined to assess the recombination kinetics and boundary layer dynamics. Despite the limitations of the model, the results give insights into the physics of recombination reactions and motivate further studies using finite-rate chemistry models. The experimental and numerical setup of the gas/gas single element rocket combustor operating with methane/oxygen is described in Section 2. Simulation results are examined in Section 3 and reaction pathways responsible for the recombination are identified. Comparisons with a frozen-chemistry flamelet model are performed to quantify the significance of recombinations on wall heat transfer augmentation.

2. Setup

2.1. Experimental configuration

The experimental configuration considered in this study corresponds to a single-element rocket combustor, operating with gaseous oxygen and gaseous methane. The experimental configuration, which is described in detail in Silvestri et al. [19,20] consists of a co-axial injector element where the oxidizer is supplied through a central jet with diameter $d_{ox} = 4$ mm, and the fuel is injected through an annulus with inner and outer diameters $d_{fu,i} = 5$ mm and $d_{fu,o} = 6$ mm respectively. The thrust chamber consists of a cylindrical combustion chamber with 12 mm diameter and a length of 285 mm as well as a nozzle with contraction ratio $\epsilon_c = 2.5$, which ensures that the Mach number in the combustion chamber is similar to typical flight configurations. The operational point chosen for the present analysis has a global oxidizer-to-fuel ratio of 2.6, a nominal operating pressure of 20 bar and the oxidizer stream is not recessed with respect to the face-plate. Thermocouples and pressure tansducers are installed along the chamber wall thereby delivering quantitative data for wall heat flux and static wall pressure.

The experimentally measured mass flow rates for the oxidizer and fuel ($\dot{m}_{O_2} = 34.82$ g/s, $\dot{m}_{CH_4} = 13.39$ g/s) as well as the corresponding inlet temperature ($T_{O_2} = 275$ K, $T_{CH_4} = 269$ K) are prescribed at the inlets and a pressure outlet is imposed at the exhaust plane. All other boundaries are defined as no-slip walls. For the thermal boundary condition at the chamber wall, the wall temperature values obtained by the inverse method of Perakis et al. [21] are applied, whereas the face-plate and injector tip are adiabatic. For the wall boundary conditions, a wall function has been used. An overview of the computational setup is given in Fig. 1. The mesh consisting of 17 million cells with 25 points across the injector lip was used for the simulation and is shown in Fig. 2. The minimum wall spacing along the chamber wall is 30 μm and a wall model was used for the viscous sublayer [22].

2.2. Governing equations

For the 3D simulations presented in the following sections, the Favre-averaged governing equations for continuity, momentum and energy are

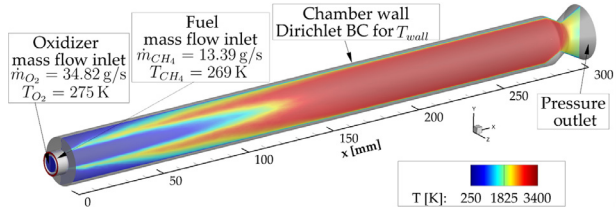

Fig. 1. Overview of the computational domain and boundary conditions.

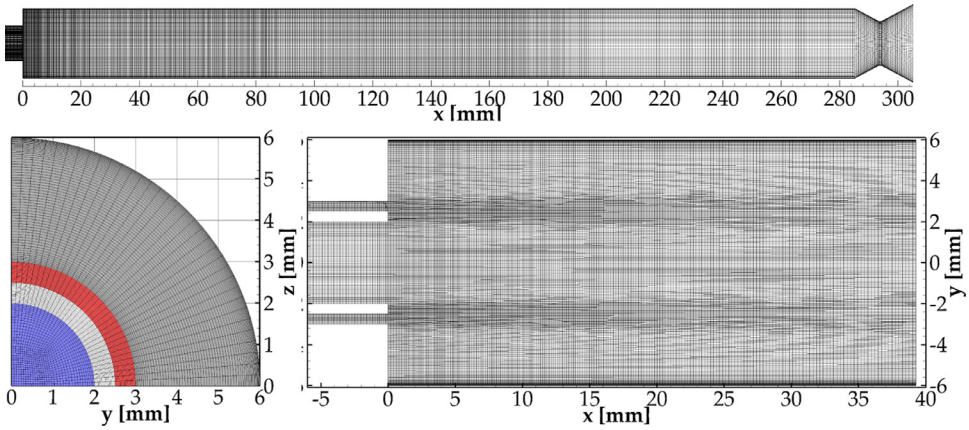

Fig. 2. Computational mesh used in the LES: side view (top), face-plate and $z = 0$ cut-plane (bottom).

solved:

$$\partial_t \bar{\rho} + \nabla \cdot (\bar{\rho}\widetilde{\boldsymbol{u}}) = 0 \tag{1}$$

$$\partial_t (\bar{\rho}\widetilde{\boldsymbol{u}}) + \nabla \cdot (\bar{\rho}\widetilde{\boldsymbol{u}}\widetilde{\boldsymbol{u}}) = -\nabla \cdot (\bar{p}\boldsymbol{I}) + \nabla \cdot (\bar{\boldsymbol{\tau}}_v + \bar{\boldsymbol{\tau}}_{SGS}) \tag{2}$$

$$\partial_t (\bar{\rho}\widetilde{E}) + \nabla \cdot [\widetilde{\boldsymbol{u}}(\bar{\rho}\widetilde{E} + \bar{p})] = \nabla \cdot [(\bar{\boldsymbol{\tau}}_v + \bar{\boldsymbol{\tau}}_{SGS}) \cdot \widetilde{\boldsymbol{u}}] - \nabla \cdot (\bar{\boldsymbol{q}}_v + \bar{\boldsymbol{q}}_{SGS}) \tag{3}$$

where ρ is the density, $\boldsymbol{u}$ is the velocity vector, p is the pressure, $\boldsymbol{\tau}$ is the viscous tensor, $\dot{\boldsymbol{q}}$ is the heat flux and E is the specific total energy combining the specific internal energy and the kinetic energy $\widetilde{E} = e + \frac{1}{2}|\widetilde{\boldsymbol{u}}|^2$ as defined in Williams [23]. Because of the low chamber pressure in the chamber which does not exceed 20bar, effects of intermolecular forces and volume correction are neglected in the definition of the energy and the ideal gas equation of state is used as closure for the system of equations.

The equations are discretized based on a finite-volume formulation and a fourth-order non-dissipative scheme is used for the convective flux discretization with a strong stability-preserving third-order Runge–Kutta scheme for time advancement [24].

2.3. Combustion modeling

To perform the LES calculation of this configuration, the Favre-filtered compressible Navier–Stokes equations are solved. A non-adiabatic flamelet progress variable (FPV) model is employed to obtain the thermo-chemical state. This model requires the solution of the filtered conservation equations for the mixture fraction, progress variable and mixture fraction variance:

$$\partial_t (\bar{\rho}\widetilde{Z}) + \nabla \cdot (\bar{\rho}\widetilde{\boldsymbol{u}}\widetilde{Z}) = \nabla \cdot \left[\left(\bar{\rho}\widetilde{D} + \frac{\mu_t}{Sc_t} \right) \nabla \widetilde{Z} \right] \tag{4}$$

$$\partial_t (\bar{\rho}\widetilde{C}) + \nabla \cdot (\bar{\rho}\widetilde{\boldsymbol{u}}\widetilde{C}) = \nabla \cdot \left[\left(\bar{\rho}\widetilde{D} + \frac{\mu_t}{Sc_t} \right) \nabla \widetilde{C} \right] + \overline{\dot{\omega}}_C \tag{5}$$

$$\partial_t (\bar{\rho}\widetilde{Z''^2}) + \nabla \cdot (\bar{\rho}\widetilde{\boldsymbol{u}}\widetilde{Z''^2}) = \nabla \cdot \left[\left(\bar{\rho}\widetilde{D} + \frac{\mu_t}{Sc_t} \right) \nabla \widetilde{Z''^2} \right] + 2\frac{\mu_t}{Sc_t} |\nabla \widetilde{Z}|^2 - \bar{\rho}\tilde{\chi} \tag{6}$$

In this non-adiabatic FPV model, an additional parameter, Z_{wall} is introduced to provide a parametrization of the flamelet solution with respect to wall distance. With this, the thermochemical state-space, consisting of chemical source term, heat release, thermo-viscous transport properties

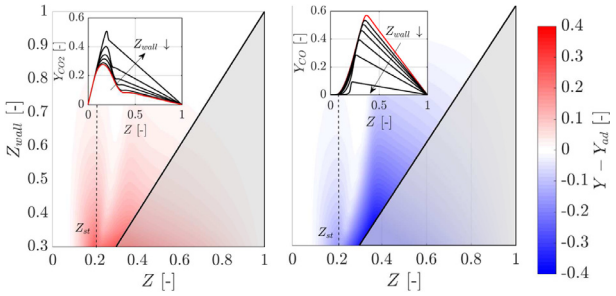

Fig. 3. CO_2 and CO mass fraction in counterflow diffusion flame calculations with the non-adiabatic wall model. Z_{wall} denotes the location of the permeable wall in mixture fraction space.

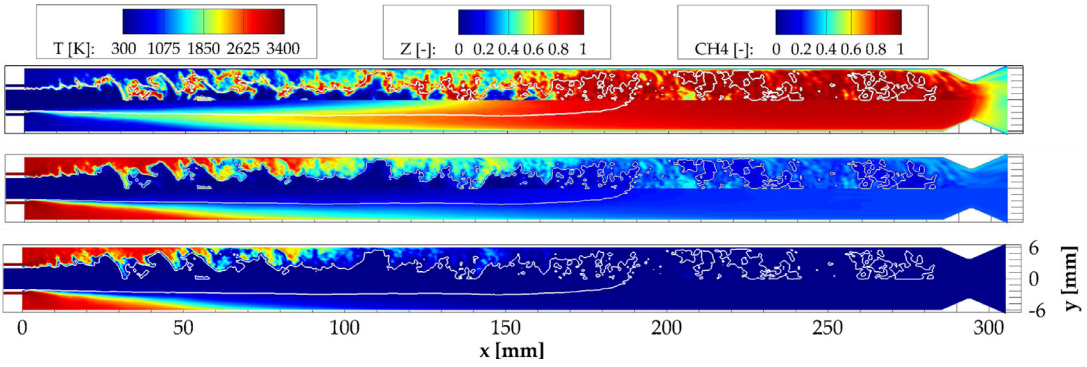

Fig. 4. Temperature, mixture fraction and methane mass fraction fields (from top to bottom) for the non-adiabatic FPV model. Upper half: instantaneous fields, bottom half: time-averaged solution. Z_{st} shown by white line.

and species mass fractions is parametrized in terms of $\widetilde{Z}$, $\widetilde{C}$, $\widetilde{Z''^2}$ and Z_{wall}, in which Z_{wall} represents the local mixture fraction at the wall. In this model, the turbulence-chemistry interaction is modeled using a presumed β-PDF and further details can be found in the work of Ma et al. [14]. The detailed GRI 3.0 mechanism is used, consisting of 35 species and 192 reactions [25]. For the closure of the turbulent viscosity μ_t the Vreman subgrid-scale model [26] is applied and a constant turbulent Schmidt number equal to 0.7 is used.

Moving the permeable wall from the fuel stream towards the flame increases the heat loss, meaning that lower values of Z_{wall} correlate to a larger enthalpy deficit and a lower temperature. At the same time, the CO mass fraction is also reduced with increasing heat loss compared to the adiabatic profile, which corresponds to the solution for $Z_{wall} = 1$.

The effect of the increased heat loss on the species mass fraction is depicted in Fig. 3, where the differences in CO and CO_2 mass fractions with respect to the adiabatic flamelet solution are plotted in mixture fraction space for different values of Z_{wall}. The line plots (shown as inlay) illustrate the evolution of the species mass fractions with varying Z_{wall}, with the red line corresponding to the adiabatic solution. The contour plots in the same figure show the deviation from the adiabatic profile ($Z_{wall} = 1$). The results correspond to a scalar dissipation rate of $\chi = 1\text{s}^{-1}$.

The black line in Fig. 3 represents the location of the permeable non-adiabatic wall. As expected, the lower enthalpy environment facilitates a significant reduction in CO mass fraction with a corresponding increase in CO_2. In the region close to stoichiometry ($Z_{st} = 0.2$) as well as the fuel-rich region an appreciable degree of CO recombination can be observed. This is explained by the larger concentration of carbon-containing species compared to the oxidizer-rich side [16]. In the following we will examine the impact of CO recombination on wall heat transfer and combustion in rocket engines.

3. LES results

Instantaneous and time-averaged flow-field results for temperature, mixture fraction and methane mass fraction are shown in Fig. 4. The injection without recess and the velocity ratio of the propellants ($u_{CH_4}/u_{O_2} \approx 0.92$) suppresses the mixing. The shear layer downstream of the injector

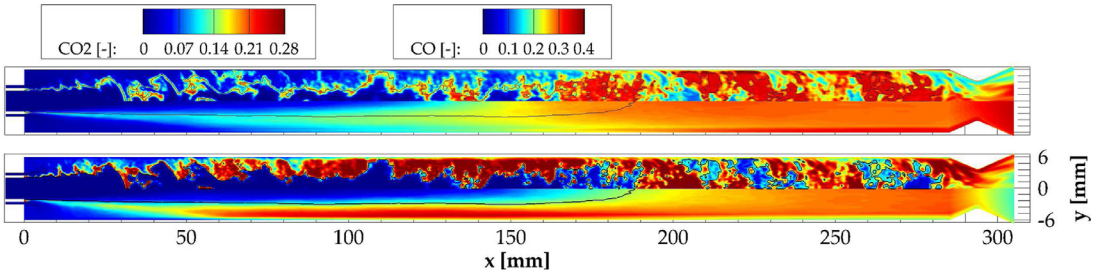

Fig. 5. CO_2 and CO mass fractions fields for the non-adiabatic FPV model. Upper half: instantaneous fields, bottom half: time-averaged solution. Z_{st} shown by black line.

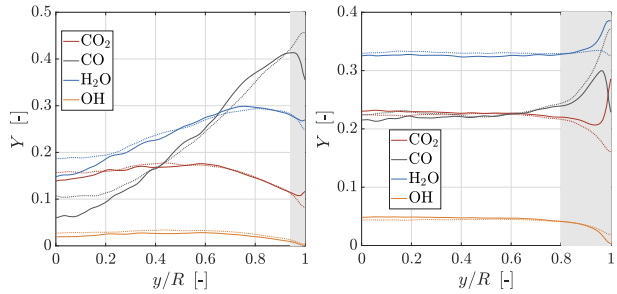

Fig. 6. Species profiles along the wall normal direction at $x = 150$ mm (left) and $x = 250$ mm (right). Dotted lines correspond to the frozen FPV model and solid lines to the non-adiabatic FPV. The gray area represents the thermal boundary layer.

exhibits small-scale Kelvin–Helmholtz instabilities, which grow with increasing axial distance. This leads to a significant radial expansion of the flame close to $x = 50$ mm and an increase in the turbulence level downstream. The stoichiometric composition ($Z_{st} = 0.2$) represented by a white line extends up to $x \approx 200$ mm, indicating a sufficient degree of mixing in the chamber. Moreover, the formation of thermal boundary layer is visible, which is a result of the enthalpy loss to the wall.

The methane, which is supplied by the outer annulus of the co-axial injector is dominant in the near-injector recirculation region but rapidly mixes and is consumed within the first half of the domain. This is also shown by the mixture fraction, with fuel-rich mixture dominating the near-wall region and oxygen-rich mixture being accumulated close to the central axis. As the mixing is enhanced however, the composition of the gas exiting the domain approaches the global mixture fraction value of 0.278. Using the definition of Danckwerts [27], an unmixedness value equal 0.021 is found at the exit plane.

The species fields of CO and CO_2 are shown in Fig. 5. It can be seen that close to the injection plane, CO and CO_2 are being formed in the reacting shear layer. As the flame expands, the CO mass fraction increases toward the radial direction closer to the wall. This is explained by the absence of oxygen near the wall to produce CO_2. With enhanced mixing, however, the CO and CO_2 exit the combustor in a more homogeneous way. Apart from the effects that the injector design and the energy release have on the CO and CO_2 mass fractions, the effect that the heat loss promotes recombination reactions can be seen near the wall throughout the domain. Specifically, a thin boundary layer is formed, where CO is converted to CO_2. The locations where recombination takes place coincide with the regions with enthalpy defect, which is defined as the difference between the local enthalpy and the adiabatic mixing enthalpy.

To elucidate the effect that the heat loss has on the species profiles, plots of the major species as a function of the wall normal direction are shown in Fig. 6. Two representative locations at $x = 150$ mm and $x = 250$ mm were chosen. The first axial position is located within the main reaction zone, while the second position is in the post-reaction zone where combustion is completed and hence the heat loss effects can be isolated. In order to quantify the effect of the recombination reactions, a simulation using the adiabatic FPV model was also carried out. For this simulation the value of Z_{wall} was set to 1. This is labeled as "frozen" model as the gas composition is unaffected by the enthalpy loss.

For both axial locations, the results obtained by the two models are in good agreement away from the wall, with small discrepancies appearing close to the chamber axis. These discrepancies occur due

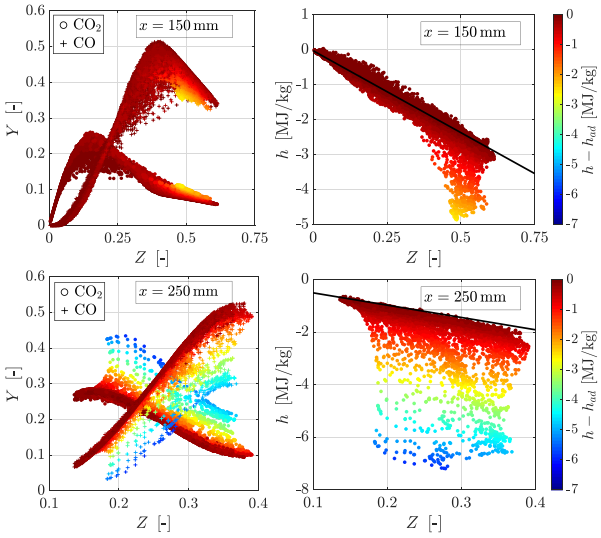

Fig. 7. Scatter plot for CO_2, CO mass fractions and enthalpy defect at $x = 150$ mm (top) and $x = 250$ mm (bottom) for the non-adiabatic FPV model. The black solid line represents the adiabatic enthalpy.

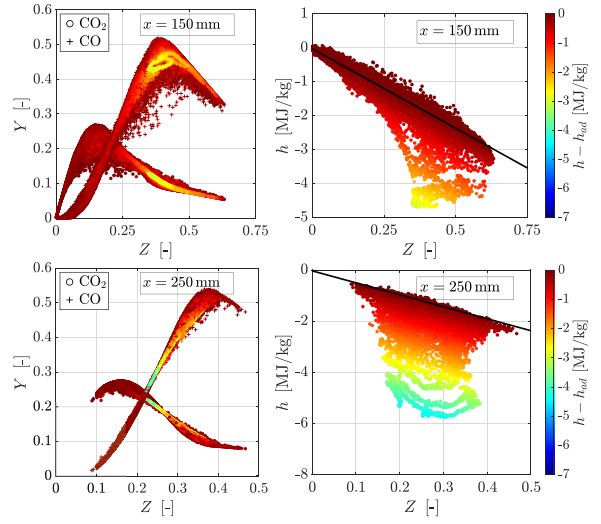

Fig. 8. Scatter plot for CO_2, CO mass fractions and enthalpy defect at $x = 150$ mm (top) and $x = 250$ mm (bottom) for the frozen FPV model. The black solid line represents the adiabatic enthalpy.

to higher heat flux obtained with the non-adiabatic FPV-solution which results in an increase in the flame length and hence a change in the gas composition along the center-line. For the first axial location, the CO mass fraction increases with decreasing distance from the wall, with a corresponding decrease in CO_2 mass fraction. This is explained by the design of the injector as shown in Fig. 5. Close to the wall, however, for $y/R > 0.9$, a species boundary layer forms, with a clear recombination of CO to CO_2 and an increase in H_2O mass fraction. For the second axial position, a homogeneous profile is observed for $y/R < 0.6$ indicating equilibrated composition. Already at $y/R = 0.8$, large deviations between the two models occur. As the thickness of the thermal boundary layer increases, the region affected by the enthalpy-defect-induced recombination broadens.

The effect of the enthalpy defect on the species composition is also illustrated in Figs. 7 and 8, where a scatter plot of the species and enthalpy defect are shown in mixture fraction space for the non-adiabatic and frozen FPV models respectively. As already established in Fig. 6, the heat loss and

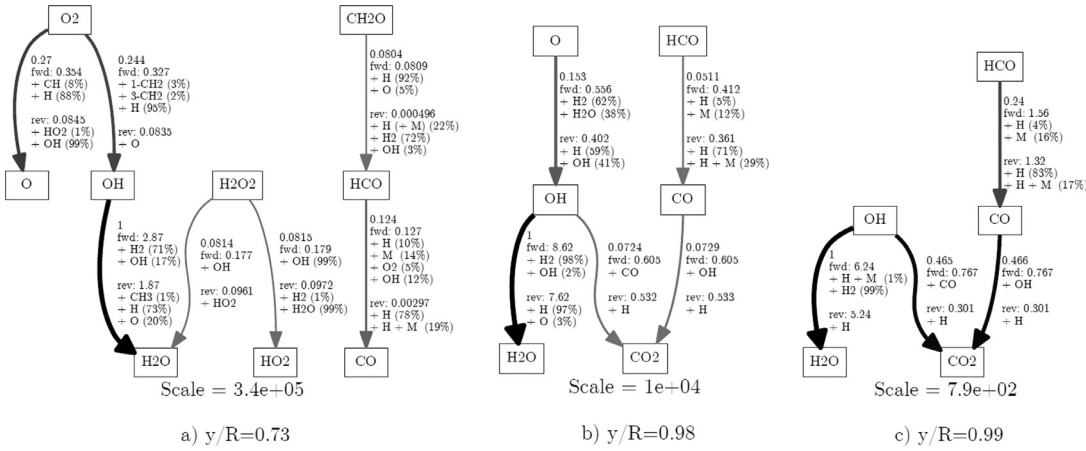

Fig. 9. Reaction path diagram at different radial locations at $x = 250$ mm. The normalized net, forward and backward atomic flux rates for the oxygen atom are included along the connecting arrows.

the recombination reactions are becoming more pronounced with increasing axial distance. This is confirmed by the large enthalpy defect at $x = 250$ mm compared to $x = 150$ mm and a resulting large degree of scattering for the CO_2 and CO mass fraction in Fig. 7. On the contrary, in the frozen model, the species mass fractions are unaffected by the low-enthalpy environment, as the scatter plot in Fig. 8 indicates.

To understand the reactions leading to the CO recombination a reaction path diagram for the oxygen atom in the non-adiabatic FPV model is performed. Results for this analysis are illustrated in Fig. 9 at three different distances from the wall for $x = 250$ mm. Before the onset of the species boundary layer ($y/R = 0.73$), the mixture is still reacting, mainly forming H_2O and CO as well as some radicals due to the high temperature combustion environment. In contrast at $y/R = 0.98$ and $y/R = 0.99$, the conversion of the previously formed CO to CO_2 and the recombination of OH to H_2O become dominant. Based on the normalized reaction rates shown in the flux diagram of Fig. 9, the reactions mainly responsible for the recombination reactions are $OH + CO \rightleftharpoons CO_2 + H$ and $H_2 + OH \rightleftharpoons H + H_2O$. As both of these reactions are exothermic, this results in a net energy release in the boundary layer, which increases the wall heat loads.

The net effect of these exothermic reactions is quantified in Fig. 11 showing a comparison of pressure and heat flux profiles from the two models along with experimental measurements [20,21]. Results from the non-adiabatic FPVA model are in good agreement with measurements. The absolute pressure level is correctly predicted with a value of approximately 18.75 bar close to the face-plate and 18 bar at the end of the combustion chamber. Apart from the absolute level, the pressure drop, which is an indicator of the acceleration and hence energy release in the combustion zone, demonstrates a satisfactory agreement with the measurements.

Within the first 30 mm from the face-plate, simulations and experiment show an increase in pressure. This is a result of the recirculation zone formed in the vicinity of the injector, feeding fuel-rich mixture directly towards the liner. After the location of peak pressure, the reduction in pressure is associated with an acceleration of the flow due to the exothermic combustion reactions. The slope of this pressure drop appears to flatten at $x \approx 200$ mm. This flattening of the pressure profile indicates a slower acceleration, and therefore a reduced heat release that characterizes the end of combustion. The location at which the change in slope occurs is in agreement with the experimentally obtained results.

The location where the chemical conversion is completed can also be inferred from the heat flux profile. Specifically, at $x = 200$ mm the maximum heat flux is observed. Subsequently for positions further downstream, the hot combustion products are cooled and the thermal boundary layer broadens, leading to a reduction in the wall heat transfer rate. Both the location and the value of the maximum heat flux (~ 7 MW/m^2) are within the experimental uncertainties.

The recirculation zone also impacts the wall heat flux values and is characterized by an increase in the local heat transfer rate at the stagnation point. After that, the heat load increases steadily before reaching the aforementioned maximum at the end of the combustion zone. Although the frozen results demonstrate a similar axial evolution of the heat flux, the absolute level is underestimated by 15%. This can be interpreted as a direct effect of the heat release resulting from the recombination reactions at the wall.

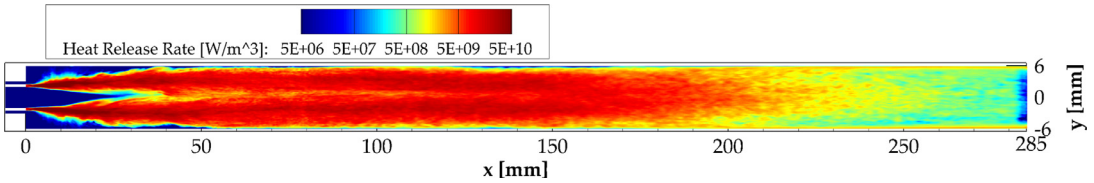

Fig. 10. Heat release rate in the combustion chamber.

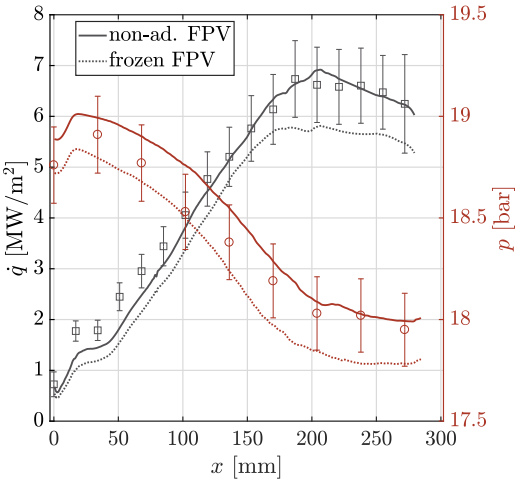

Fig. 11. Comparison of simulation results with measurements for azimuthally averaged wall heat transfer and pressure profiles.

A direct confirmation of the fact that the end of combustion occurs at approximately $x = 200$ mm is provided by the heat release rate in Fig. 10. Specifically, the bulk of the heat release appears to be taking place within the shear layer downstream of the coaxial injector. At locations further downstream, where the mixing and the combustion is completed, a gradual reduction in the heat release is observed. This decrease in the heat release is most prominent for axial locations larger than 200 mm and coincides with the experimental heat flux and pressure measurements. It is important to note that in regions where the gas is homogeneously mixed and the bulk energy release is completed, the recombination reaction in the boundary layer zone remain appreciable. In fact due to the continuing exothermic recombination reactions close to the wall, additional heat is released, thereby directly affecting the wall heat load.

4. Conclusions

A non-adiabatic flamelet model is utilized for the simulation of a methane/oxygen sub-scale rocket combustor. Comparisons with experimental results show a good agreement for both the heat flux and the pressure profiles. Simulation results are analyzed to examine the impact of CO recombination on heat flux and combustion performance.

In the low-enthalpy environment of the boundary layer the hot products recombine to form CO_2 and H_2O. These recombination reactions are exothermic and can noticeably increase the wall heat loads. By comparing the results with simulations employing frozen chemistry, it is shown that the overall contribution of the recombination to the total heat release amounts to approximately 15%. The critical reaction pathways are identified, showing that $OH + CO \rightleftharpoons CO_2 + H$ and $H2 + OH \rightleftharpoons H + H_2O$ are the main pathways.

These results illustrate the relevance of considering finite-rate chemistry and recombination reactions for the prediction of CH_4/O_2 rocket combustion. The insights given by the non-adiabatic model motivate more detailed investigations of the chemical pathways and time-scales of the reacting boundary layer in sub-scale hydrocarbon engines using DNS and finite-rate chemistry. Moreover, further analysis of the turbulent boundary-layer structure and vortex-dynamics is needed as it pertains to modeling needs for WMLES.

Declaration of Competing Interest

The authors declare that they have no known competing financial interests or personal relationships that could have appeared to influence the work reported in this paper.

Acknowledgements

The authors gratefully acknowledge the Gauss Centre for Supercomputing e.V. for providing computing time on the supercomputer SuperMUC at Leibniz Supercomputing Centre. Financial support has been provided by the Bavaria California Technology Center and the German Research Foundation (DFG) in the framework of the SFB TRR40. MI acknowledges support through AFOSR (Award No. FA9300-19P-1502) and NASA (Award No. NNX17CS15P).

References

[1] J.C. Melcher, R.L. Morehead, *AIAA Paper* (2014), doi:10.2514/6.2014-3681.

[2] A. Iannetti, N. Girard, N. Ravier, E. Edeline, D. Tchou-Kien, *AIAA Paper* (2017), doi:10.2514/6.2017-4750.

[3] M. Rudnykh, S. Carapellese, D. Liuzzi, et al., *Acta Astronaut.* 126 (2016) 364–374.

[4] O.J. Haidn, Advances on Propulsion Technology for High-Speed Aircraft, vol. 1, Research and Technology Organisation - North Atlantic Treaty Organisation, 2008, pp. 1–6.

[5] D. Preclik, G. Hagemann, O. Knab, L. Brummer, C. Mading, D. Wiedmann, P. Vuillermoz, 2005.

[6] J.C. Oefelein, V. Yang, *J. Propul. Power* 14 (5) (1998) 843–857, doi:10.2514/2.5349.

[7] V.P. Zhukov, *J. Propul. Power* 31 (6) (2015) 1707–1714, doi:10.2514/1.B35654.

[8] G.P. Sutton, O. Biblarz, *Rocket Propulsion Elements*, John Wiley & Sons, 2016.

[9] J. Riccius, O. Haidn, E. Zametaev, *AIAA Paper* (2004), doi:10.2514/6.2004-3670.

[10] F. Hötte, T. Fiedler, M.C. Haupt, P. Lungu, C.V. Sethe, O.J. Haidn, *J. Propul. Power* 35 (5) (2019) 1–11, doi:10.2514/1.B37439.

[11] R. Schuff, M. Maier, O. Sindiy, Ulrich C., Fugger S., *AIAA Paper* (2006), doi:10.2514/6.2006-4534.

[12] O. Cabrit, F. Nicoud, *Phys. Fluids* 21 (5) (2009) 055108.

[13] B. Betti, D. Bianchi, F. Nasuti, E. Martelli, *AIAA J.* 54 (1) (2016) 1693–1703, doi:10.2514/1.J054606.

[14] P.C. Ma, H. Wu, M. Ihme, J.-P. Hickey, *AIAA J.* 56 (6) (2018) 2336–2349, doi:10.2514/1.J056539.

[15] P. Breda, M. Pfitzner, N. Perakis, O. Haidn, in: Proceedings of the EUCASS, 2019.

[16] N. Perakis, C. Roth, O.J. Haidn, in: Proceedings of the Space Propulsion Conference, 2018.

[17] J. Zips, C. Traxinger, M. Pfitzner, *Int. J. Heat Mass Transf.* 143 (2019) 118474.

[18] D. Maestro, B. Cuenot, L. Selle, *Flow Turbul.Combust.* 103 (2019) 1–32.

[19] S. Silvestri, M. Celano, O. Haidn, O. Knab, in: Proceedings of the EUCASS, 2015.

[20] S. Silvestri, M.P. Celano, C. Kirchberger, G. Schlieben, O. Haidn, O. Knab, *Trans. JPN Soc. Aeron. Space Sci.* 14 (30) (2016) 13–20.

[21] N. Perakis, O.J. Haidn, *Int. J. Heat Mass Transf.* 131 (2019) 150–166, doi:10.1016/j.ijheatmasstransfer.2018.11.048.

[22] S. Kawai, J. Larsson, *Phys. Fluids* 25 (1) (2013) 015105.

[23] F.A. Williams, *Combustion Theory*, CRC Press, 2018.

[24] P.C. Ma, Y. Lv, M. Ihme, *J. Comput. Phys.* 340 (2017) 330–357, doi:10.1016/j.jcp.2017.03.022.

[25] G.P. Smith, D.M. Golden, M. Frenklach, *GRI-Mech 3.0,* (2000). http://combustion.berkeley.edu/gri-mech/

[26] A. Vreman, *Phys. Fluids* 16 (10) (2004) 3670–3681, doi:10.1063/1.1785131.

[27] P. Danckwerts, *App. Sc. Res. Sec. A* 3 (4) (1952) 279–296, doi:10.1007/BF03184936.